Novel insights into the charge storage mechanism in pseudocapacitive vanadium nitride thick films for high-performance on-chip micro-supercapacitors

Kevin Robert, Didier Stiévenard, D. Deresmes, Camille Douard, Antonella Iadecola, David Troadec, Pardis Simon, Nicolas Nuns, Maya Marinova, Marielle Huvé, et al.

Novel insights into the charge storage mechanism in pseudocapacitive vanadium nitride thick films for high-performance on-chip micro-supercapacitors

Kevin Robert[1,2], Didier Stiévenard[1], Dominique Deresmes[1], Camille Douard[2,3], Antonella Iadecola[2], David Troadec[1], Pardis Simon[4], Nicolas Nuns[4], Maya Marinova[4], Marielle Huvé[4], Pascal Roussel[4], Thierry Brousse[2,3*] and Christophe Lethien[1,2*]

[1]Institut d'Electronique, de Microélectronique et de Nanotechnologies (IEMN), Université de Lille, CNRS, Centrale Lille, ISEN, Université de Valenciennes, UMR 8520 - IEMN, F-59000 Lille, France

[2]Réseau sur le Stockage Electrochimique de l'Energie (RS2E), CNRS FR 3459, 33 rue Saint Leu, 80039 Amiens Cedex, France

[3]Institut des Matériaux Jean Rouxel (IMN), CNRS UMR 6502 – Université de Nantes, 2 rue de la Houssinière BP32229, 44322 Nantes cedex 3, France

[4]Unité de Catalyse et de Chimie du Solide (UCCS), Fédération Chevreul, Université de Lille, CNRS, Centrale Lille, ENSCL, Université d'Artois, UMR 8181 – UCCS, F-59000 Lille, France

*Correspondence to: **christophe.lethien@univ-lille.fr** & **thierry.brousse@univ-nantes.fr**

Abstract

The *Internet of Things*, enabled by a worldwide network of interconnected sensors, is limited in its large-scale deployment of nomadic miniaturized devices due to the bounds of energy self-sufficiency. One possible solution, albeit challenging, is constructing on-chip pseudocapacitive micro-supercapacitors. Herein, we achieve the collective fabrication of micro-supercapacitors based on sputtered bi-functional vanadium nitride films. Our reported surface and volumetric capacitance values (1.2 F cm^{-2} and > 700 F cm^{-3}, respectively) compete well with those of cutting-edge transition metal oxide/nitride materials, and exceed those of standard carbon electrodes. The pseudocapacitive behavior of vanadium nitride in aqueous electrolyte remaining unclear, research involving *in situ/operando* characterization techniques on sputtered vanadium nitride film in aqueous electrolyte was conducted — thus enabling us to unveil its charge storage process here.

Introduction

Secondary batteries [1] are conventional electrochemical energy storage systems used to power nomadic devices. Unfortunately, the mobility of such devices is limited by lengthy charging times and a deterioration in battery performance at upwards of a few thousand cycles. The Internet of Things (IoT) is a revolutionary technology aimed at creating an ecosystem of interconnected devices in order to improve our daily lives [2]. Autonomy and mobility are crucial parameters with respect to powering IoT micro-devices, and energy storage systems capable of delivering high energy density at high charge / discharge rates are a fundamental prerequisite for next-generation IoT networks [3]. Lithium micro-batteries (MBs) [4,5] and carbon micro-supercapacitors (MSCs) [6–8] are currently the most viable candidates for powering smart and miniaturized sensors. Regarding the former, such MBs are hampered by the low charge / discharge rates whereas the latter are limited to the low capacitance of the carbon electrodes. MSCs based on pseudocapacitive materials are a class of electrochemical capacitors where fast redox reaction occur near the surface of the electrode material [9–12], providing higher energy densities than carbon-based MSCs. However, the main issue with these is designing a pseudocapacitive material that combines rapid ion diffusion and fast electron transport in thick electrodes. Following the discovery of the pseudocapacitive properties of RuO_2 [13], numerous transition metal oxides – TMO – (MnO_2, T-Nb_2O_5….) [14–19] and a two-dimensional transition metal carbide — namely MXene [20–22] — were investigated. Whereas TMOs show low electrical conductivity, MXene combine rapid electron transport in the 2D metal carbide with fast redox reactions at the TMO-like surface. However, depositing MXene films using deposition methods issuing from the microelectronics industry proves challenging when a scale-up of the technology is required.

Transition Metal Nitrides (TMN) are a widely-studied class of materials owing to their favorable electrical and electrochemical properties. Molybdenum and vanadium nitrides [23,24] clearly demonstrated outstanding pseudocapacitive properties (> 700 F g^{-1}) in aqueous electrolyte, even though the charge storage mechanism of vanadium nitride remained unclear [24,25]. Sputtered bi-functional vanadium nitride (VN) film was shown to be an intrinsically efficient current collector and electrode material for on-chip MSCs due to its electrochemical and electrical properties [12]. This sputtering based-strategy clearly facilitates the scaling up of the technology, by following the same roadmap that we recently proposed for on-chip MSCs based on nanoporous carbon-derived carbide films [6]. Herein, various scientific issues ranging from fundamental concerns to the technological fabrication of MSCs on a silicon wafer are addressed. The charge storage process occurring in sputtered VN films is thoroughly investigated in order to explain their remarkably high areal and volumetric capacitances. To this end, we employed a combination of numerous advanced characterization techniques such as *Operando* X-Ray Absorption Spectroscopy under synchrotron radiation, as well as powerful surface techniques like X-ray Photoelectron Spectroscopy (XPS) coupled with Time-of-Flight Secondary Ion Mass Spectrometry (ToF-SIMS) and Electron Energy Loss Spectroscopy (EELS) analysis at the nanoscale in a Transmission Electron Microscope (TEM). Our findings show that we have succeeded in extending the limits of VN films deposited via production-compatible microelectronic deposition methods in order to attain the highest areal (1.2 F cm^{-2}) and volumetric (> 700 F cm^{-3}) capacitance values hitherto reported, to our knowledge, in the domain of MSCs in aqueous electrolyte. Additionally, *in situ* Atomic Force Microscopy (AFM) imaging of VN-based MSCs revealed their favorable cycling behavior (~ 50 000 cycles). It can thus be concluded that the performance of these MSCs certainly

fulfills the requirements of IoT miniaturized devices in terms of rate capabilities and long-term cycling.

Charge Storage mechanism in vanadium nitride films

Figure 1A depicts the used strategy to investigate the charge storage process in sputtered VN films. To maximize the film capacitance, it is important to clearly identify and understand the key role of the sputtering temperature on the VN morphology. SEM cross-section analysis and AFM top-surface imaging of the 340 nm-thick sputtered VN films are reported in **Figure 1B** and **Figure S1** vs the heating temperature. The higher the temperature, the higher the ad-atoms' mobility [12,26], the lower the inter-columnar spacing. At 20 °C, the RMS roughness was 3.9 nm indicating the homogeneity of the film's surface (**Figure 1C**). For higher temperatures, the roughness increased up to 16 nm, in good agreement with the observation of increasingly dense bright spots. These spots correspond to pyramidal patterns (**Figure 1B**).

Judging by these AFM images, and based on recent methods published by our group [27], it was deduced that the projected length, L_p (**Figure 1C**), decreased from 36 to 16.5 µm. Concurrently, the contribution of the pyramids to L_p increased from 0 up to 14 µm for high temperature deposition. The AFM images in **Figure 1D** highlight the formation of a pyramidal-type pattern at 350 °C for 2 µm-thick films, confirming the formation of pyramids at high temperatures.

Finally, based on L_p, we evaluated the specific surface, S_e, of 340-nm thick VN films (**Figure 1E)**, which decreased from 12.5 down to 5 cm^2 per cm^2 footprint as the temperature shifted from room temperature (RT) to 450 °C. Electrochemical analysis of those VN films was then conducted. As expected, the cyclic voltammogram (CV) exhibited a rectangular shape (**Figure 1F**), and the higher the temperature, the lower the CV areas. On one hand, at 5 mV s^{-1}, the capacitance

decreased from 42 to 30 mF cm^{-2} when the temperature was increased from RT to 450 °C (**Figure 1G**). On the other hand, the electrical conductivity (**Figure 1G**) increases linearly with the temperature. To maximize the specific surface, the areal capacitance while keeping sufficiently high the conductivity, the compromise consists in depositing the vanadium nitride film at 100 °C. This study confirmed the key role that temperature plays in determining pyramidal patterns, capacitance values and specific surface areas.

In order to investigate the charge storage mechanism in sputtered and crystallized VN films (**Figure S1**, Supplementary Materials (SM) section), surface analyses were initially carried out on 100 nm-thick sample. Three square-shaped craters were drilled into the VN film using the ToF-SIMS equipment. The 1st crater was bored down to the silicon substrate to assess the etching rate of the VN and Si_3N_4 layers. The 2nd crater was stopped approximately in the middle of the VN layer (≈ 50 nm), while the 3rd crater was etched down to the VN / Si_3N_4 interface (**Figure 2A & Figure S2A**). The ToF-SIMS depth profile reveals the presence of vanadium nitride, oxide and oxynitride species (**Figure 2B**). Then, the sample was transferred from the ToF-SIMS to the XPS chamber under vacuum in order to analyze the film at the surface and inside the 2nd and 3rd SIMS craters.

Figure 2C shows the high-resolution XPS spectra for V *2p* and O *1s* core levels from the surface to the VN / Si_3N_4 interface: we found an oxygen component at the surface as well as in the craters. The V *2p* core level at the VN surface is rather complex. The first contribution of the V $2p_{3/2}$ level is measured at 513.70 eV. This is consistent with the formation of the VN species. In order to fit the spectrum adequately, two additional V *2p* doublets with V $2p_{3/2}$ BE at 514.8 and 516.8 eV were required. Those peaks were observed in the V *2p* core level spectra of the 2nd and 3rd craters, but with a lower intensity as compared to the surface. As concerns the XPS, considering the presence

of oxygen and the oxynitride peak in N *1s* spectra (**Figure S2D**), the 2nd contribution can be ascribed to a vanadium (III) oxide or $VN_{1-x}O_x$ oxynitride, whereas the last peak at higher BE can be ascribed to a vanadium (IV) oxide [28]. To summarize, ToF-SIMS paired with XPS analyses confirm the presence of vanadium nitride, vanadium oxide (+III and + IV) and a small amount of vanadium oxynitride in the films, from their surface to the VN / Si_3N_4 interface.

So as to obtain further insight into the charge storage process and to refine the XPS conclusions, additional investigations were deemed necessary. The charge storage mechanism in VN nanocrystals was studied [24] by Kumta *et al* in 2006, whereby *ex situ* XPS analysis confirmed the formation of a vanadium oxide shell (0.5 nm) surrounding the vanadium nitride core of the nanocrystals. However, they found it difficult to predict the type of vanadium oxides (V_xO_y) via *ex situ* XPS analyses. To address this issue, we opted to study 1 µm-thick sputtered VN films by *operando* XAS at the V-K edge in a KOH electrolyte. Additionally, EELS/TEM analysis was carried out to identify the position of the vanadium oxide layer within the sputtered columnar vanadium nitride film. The experimental method for the *operando* XAS measurement (**Figure S3**) is detailed in the SM, where all the parameters were optimized to maximize the signal to noise ratio (**Figure S4A-F**).

The CV (2nd cycle) is shown in **Figure 3A**. Fast data acquisition of the XAS signal allows for a fine sampling of the charge storage process, so as to achieve accurate monitoring of the oxidation state of the transition metal. Absorption spectra reported in **Figure 3B** clearly highlight a shift of the absorption threshold upon charge / discharge cycling. The plot showing the energy shift of the applied potential exhibits a triangular shape (**Figure 3C**), similar to that of pseudocapacitive material [29,30]. To find the vanadium species involved in the charge storage mechanism, in **Figure 3D** we plot the evolution of the absorption edge for V_xO_y (cross points) and VN (square point)

reference compounds (**Figure S4G**) vs the valence of the vanadium element. In this graph, we also show the energy absorption edges (circular points) measured during the *operando* XAS analysis (**Figure 3B-C and S4H-I**). Not surprisingly, this graph clearly indicates that VN could not be responsible for the pseudocapacitive process — a vanadium oxide layer seems to be the key player in the fast charge transfer occurring during the redox process, confirming the hypothesis proposed by Kumta *et al*. While in 2006 we found it difficult to find the type of V_xO_y involved in the process by *ex situ* XPS [24] – as observed in our XPS / ToF-SIMS experiments – the originality of this, hitherto unreported, study deals with the accurate determination of the vanadium oxidation degree in the vanadium oxide species upon charge / discharge cycling. From these *operando* XAS measurements, the average oxidation state was found to vary from 3.56 to 3.66 (correlated with XPS analyses), meaning that the XANES capacitance is approximately 88 mF cm^{-2}. This capacitance is a perfect match with that of 1 µm-thick VN film (~ 90 mF cm^{-2}). Once we had demonstrated that a mixed vanadium oxide V_2O_3 / VO_2 – type is involved in the charge storage mechanism, the question arose as to where the V_xO_y are located within the VN film. To tackle this issue, TEM analysis and EELS spectroscopy with a nanosized-spot was performed on 7 µm-thick sputtered VN film. The **Figure 3E-F** perfectly illustrates the columnar morphology of the film. Between two VN columns, we observe brighter contrast in the TEM image and darker areas in the HAADF images**,** corresponding to porosities and/or areas with lower atomic density. **Figure 3G** shows the EELS spectra measured within the VN column (blue line) and between two VN columns (pink line). The EELS spectrum (blue line) in the VN column shows the V-$L_{3,2}$ edge at 517 eV, and the negligible intensity at 531 eV corresponding to the O-K edge. The pink line clearly indicates a shift of V-$L_{3,2}$ edge towards higher energy (518.1 eV), accompanied by a considerable

increase of the O-K edge at 531 eV. We observe a higher oxidation state of V in the area between the VN columns, corresponding to the formation of V_xO_y.

Based on these findings — finally able to fully comprehend the charge storage process involved in sputtered VN films operating in aqueous electrolyte — we reached the conclusion that the sputtered VN film acts as a conductive scaffold for electron transport, while the amorphous mixed-valence vanadium oxides (+III / + IV), located at the edge of each column, are the redox-active material allowing fast charge transfer (**Figure 1A**). This conclusion resonates with that of a previous publication investigating MXene electrodes, where the conductive carbide layer enables rapid electron transport and where the TMO-like surface is the redox-active center [22]. Such findings reaffirm the suitability of sputtered VN for MSC applications.

Electrode design providing high areal and volumetric performance

As previously demonstrated, capacitance of the VN films decreases and electrical conductivity increases at higher deposition temperatures. Consequently, an intermediate temperature of 100 °C was chosen for the sputtering deposition since, at this temperature, VN is a suitable current collector and an efficient pseudocapacitive electrode. To enhance the surface capacitance, an interesting approach is to deposit a thicker layer providing that (1) the deposition method is compatible with the microelectronics industry, and (2) that the electrical conductivity of the electrode material is sufficiently high for fast electron transport. AFM analysis is shown in **Figure 4A** where the evolution of L_p and S_e vs the film thickness is reported. The top-view and the SEM cross-section images, the roughness, the evolution of the electrical conductivity as well as the X-Ray Diffraction analyses of the VN films are shown in **Figure S5,** confirming the polycrystalline nature of the VN films (PDF card 000-035-1768) and the good conducting properties of those VN

films. The S_e is clearly enhanced to a 70 cm^2 per cm^2 footprint area for 16 µm-thick VN film. As a result, the areal capacitance is increased as depicted in the CV plots (**Figure 4B)**. Further discussion regarding the ion kinetics within the VN films is provided in the SM. As mentioned, the areal and volumetric capacitance values are remarkable and unique: a surface capacitance of up to 1.2 F cm^{-2} was measured at 5 mV s^{-1} for 16 µm-thick VN film **(Figure 4C),** which is 6 times higher than our previous results [12]. This translates into a volumetric capacitance of 700 F cm^{-3}. For thinner films, the volumetric capacitance value increases up to 1300 F cm^{-3} **(Figure 4C)**. It is noteworthy that the 16 µm-thick VN film retains more than 80 % of the initial capacitance for 50 000 cycles (**Figure 4D**). A benchmarking of the achieved areal performance (square points) as compared to state-of-the-art (pseudo)capacitive electrodes is furnished in **Figure 4E**. The 7 µm-thick carbon-derived carbide (CDC) film [31,32] delivers 0.1 F cm^{-2} in organic electrolyte [6,33]. In aqueous electrolyte [6], 5 µm-thick CDC films deliver up to 0.2 F cm^{-2}. MXene Ti_3C_2-T electrode is a very attractive material, also from the point of view of areal and volumetric capacitances: 5 µm-thick Ti_3C_2-T "clay" electrodes deliver up to a 0.4 F cm^{-2} / 900 F cm^{-3} capacitance values when measured in 1M H_2SO_4 [34]. The volumetric capacitance of a Ti_3C_2-T electrode (3 µm-thick) decreases to 400 F cm^{-3} in 1M KOH [20]. The corresponding areal capacitance value (120 mF cm^{-2}) is twice as low as the one we obtained (**Figure S6C**) with a 2.5 µm-thick VN film (> 250 mF cm^{-2} / 1000 F cm^{-3}) in 1M KOH. Moreover, one faces a similar issue here with respect to producing MXene [20,21,34] films via deposition methods that are compatible with the microelectronics industry and suitable for MSC applications. These sputtered VN films thus provide the most favorable compromise between surface and volumetric capacitances when compared to cutting-edge electrodes, while keeping the electrical conductivity high in the absence of a conductive agent in order to facilitate fast electron transport for miniaturized devices. Having reached a fundamental

understanding of the charge storage process and film optimizations, we succeeded in fabricating on-chip interdigitated MSC based on VN electrodes on a 3-inch silicon wafer. An assessment of the electrode degradation upon cycling was carried out using *in situ* AFM in 1M KOH.

Micro-supercapacitors based on VN films

CDC films [6] have already been analyzed by AFM in ionic liquid electrolyte [35] to track the volume expansion of the electrode upon cycling. To ascertain the aging of the VN electrode, we develop an experimental test setup (**Figure S7**) in order to trace the volume expansion of the interdigitated electrodes tested in 1M KOH (**Figure 5A**). A movie demonstrating the *in situ* characterization of the MSC in 1M KOH is furnished in the SM. The interdigitated topology is illustrated in **Figure 5B**, where the etching process was stopped at the VN / Si_3N_4 interface. AFM imaging of the VN electrode — firstly in the absence of liquid, then soaked in water and then in 1M KOH electrolyte, respectively — was performed prior to *in situ* analysis (**Figure S7C** and **S7D)**. The AFM images attest to the absence of volume expansion and chemical degradation in either the electrode or the AFM tip (90 minutes test). We then studied the degradation of the VN film upon cycling in 1M KOH by applying a voltage plateau from -0.4 V down to -1 V vs Hg/HgO (and inversely) for 2 minutes on the 1st electrode (**Figure 5B).** The 2nd electrode remained unbiased so as to compare the potential volume expansion. From cross-section AFM images, we measured the thickness of the VN operating electrode, using the Si_3N_4 surface as a reference (**Figure 5C**). The thickness of the VN electrode is shown to remain constant regardless of the applied potential, *i.e.* there is no expansion of the VN electrode upon cycling, validating the long-term cycling (50 000 cycles). Finally, the performance of on-chip MSCs are evaluated. Galvanostatic charge / discharge cycling is shown in **Figure 5D**. The energy densities of 7 µm-thick and 16 µm-thick MSCs (Ragone plot

- **Figure 5E**) reach 10 and 25 µWh cm^{-2}, respectively. The 16-µm thick MSC exhibits an energy density which is 16 times higher that of MSCs based on CDC films [6] tested in 1M H_2SO_4. The maximum power density remains stable at around 4 mW cm^{-2}, regardless of film thickness.

Our work provides a fresh perspective on the charge storage mechanism of sputtered VN films in KOH electrolyte. We succeed in fine-tuning the VN properties in order to synthesize bi-functional films (i.e. for use as both current collector & electrode material for on-chip MSCs). These bi-functional VN thick films (16 µm) exhibit both high specific area (70 cm^2 per cm^2) and areal capacitance (1.2 F cm^{-2}), as well as both high volumetric capacitance (> 700 F cm^{-3}) and capacitance retention (50 000 cycles). It is noteworthy that these MSCs are constructed using a CMOS-compatible microfabrication technique and tested using *in situ* AFM methods to verify cycling stability. In light of the above, the present study clearly paves the way for the collective fabrication of miniaturized energy storage devices on a silicon wafer, and thus for the efficient powering of next-generation IoT micro-devices.

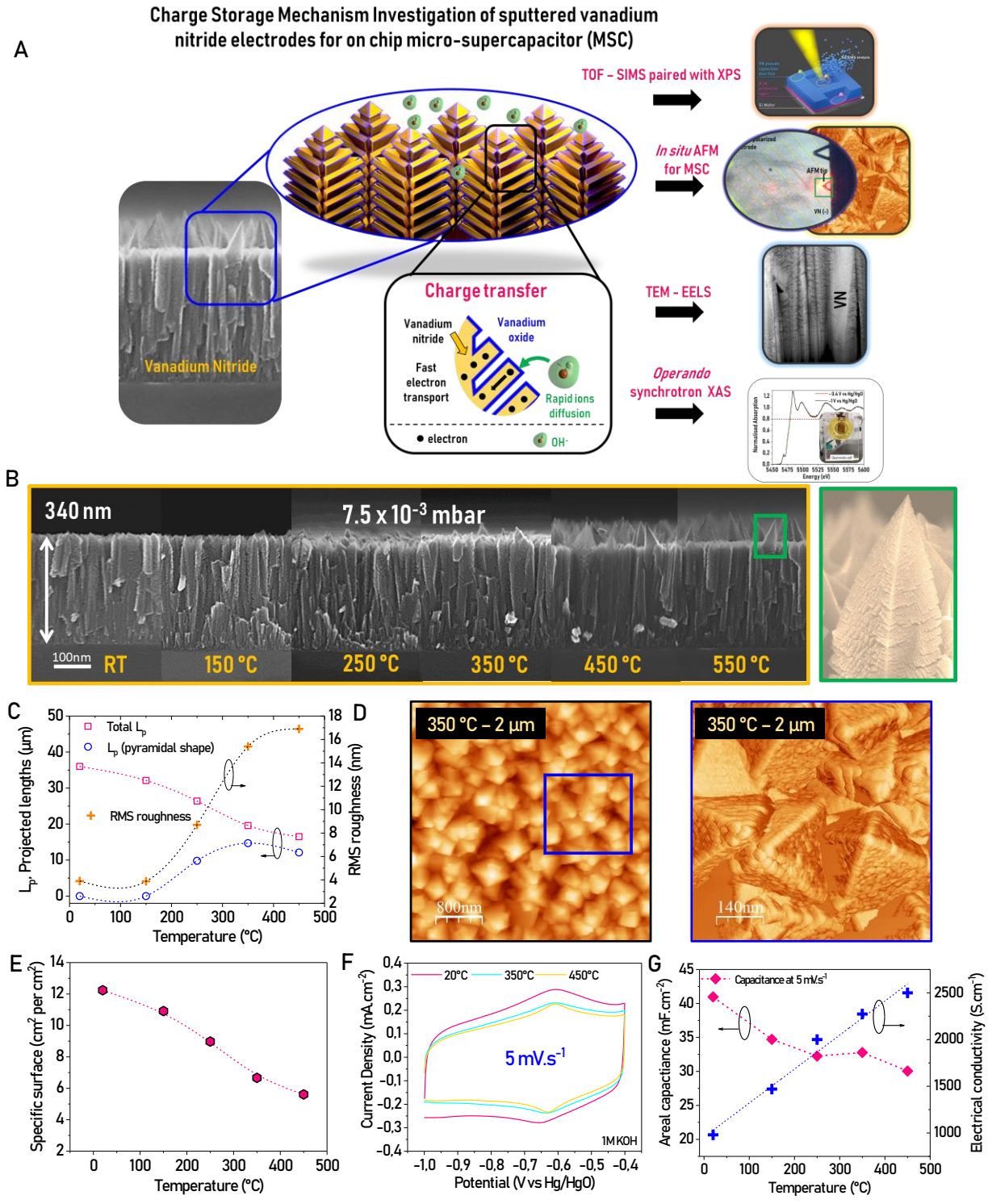

Figure 1 – A. Overview of the strategy used to study the charge storage process. **B.** SEM cross-section imaging of the VN films. **C.** Plots of L_p and roughness vs the temperature. **D.** AFM top

surface and amplitude error imaging of the 2 µm-thick VN films deposited at 350 °C. **E.** Evolution of S_e vs the temperature. **F.** CV profile of the 340 nm-thick VN films vs the deposition temperature at 5 $mV.s^{-1}$ in 1M KOH. **G.** Evolution of the areal capacitance at 5 $mV.s^{-1}$ and the electrical conductivity vs temperature.

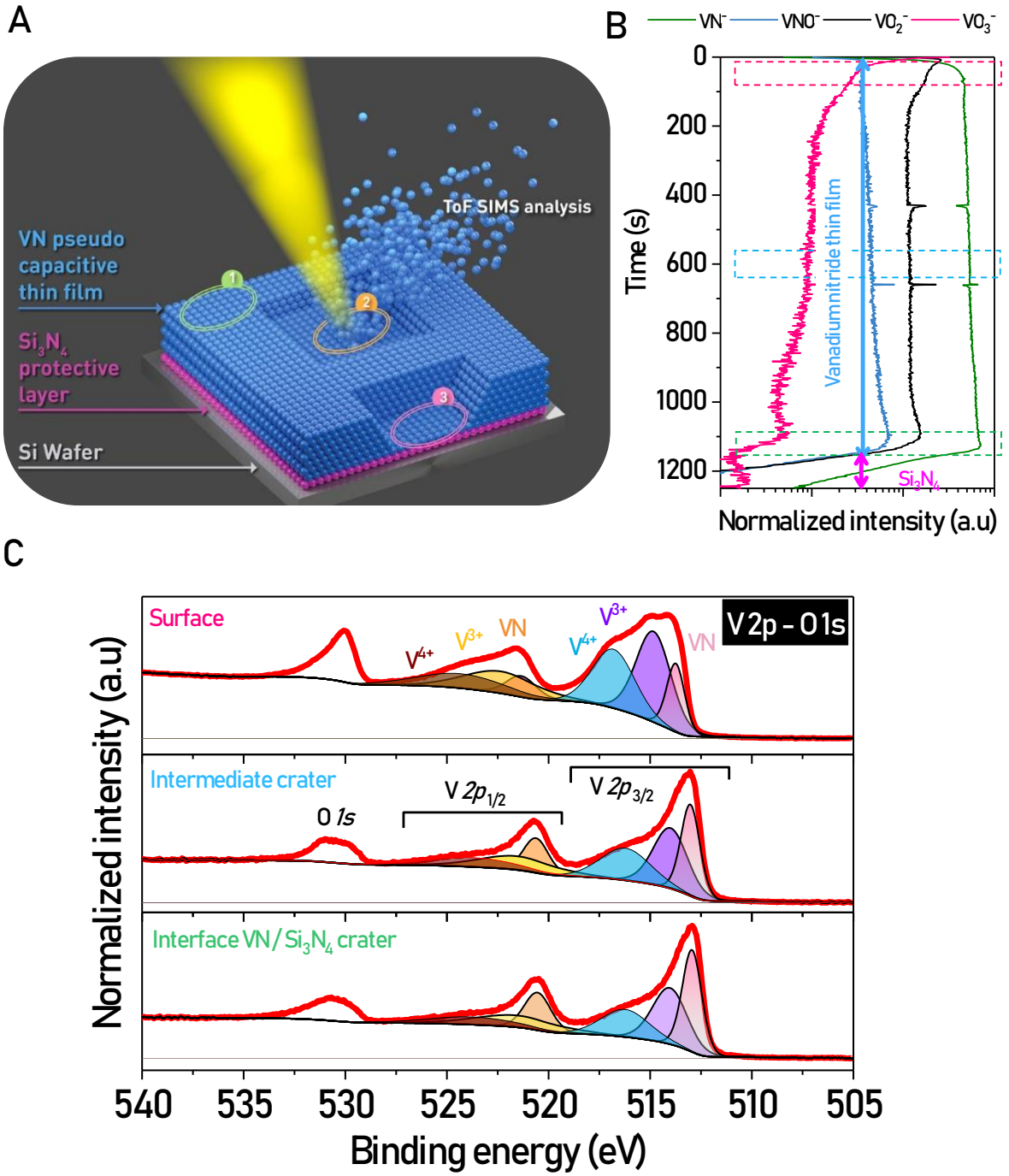

Figure 2 – A. Overview of the combined ToF-SIMS / XPS analyses at the surface, in the middle of the VN film, and at the VN / Si_3N_4 interface. **B.** ToF-SIMS depth profile of the VN film from

the surface to the VN / Si_3N_4 interface. **C.** High resolution XPS spectra (V *2p* – O *1s* core-level region) of the VN film.

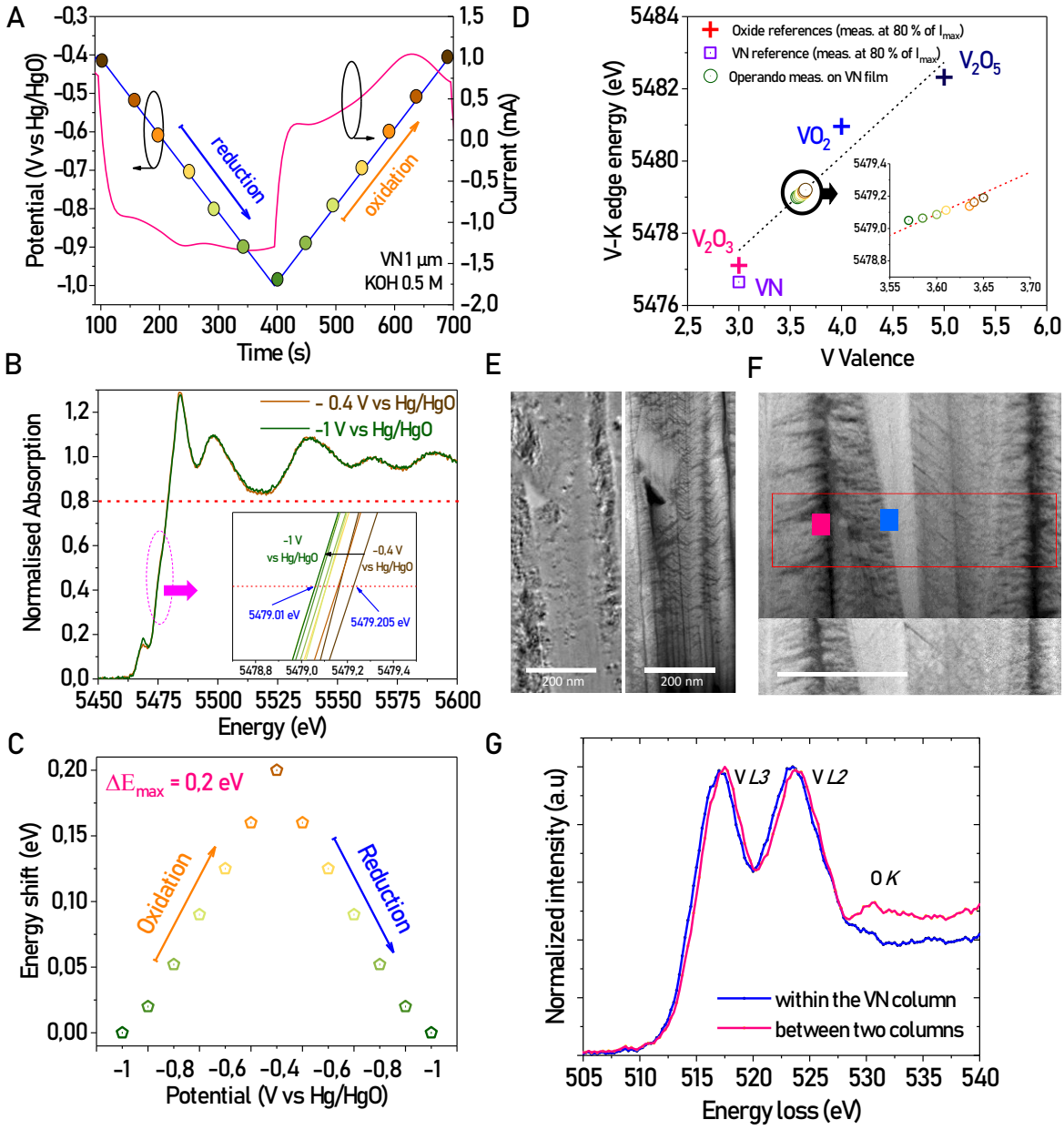

Figure 3 – Investigation of the Charge Storage Mechanism in the sputtered VN Films. **A.** Plots of the current (pink line) and the potential (blue line) vs the time. **B.** V K-edge XANES spectra of the VN electrode; the inset represents a focus of the edge position at 80 % of edge step when the potential varies between -0.4 and -1.0 V vs Hg/HgO (reduction process). **C.** Energy shift as a function of the working potential, highlighting the oxidation and reduction processes. **D**. Plots of the energy position during the oxidation process as a function of the vanadium valence. **E.** TEM

and HAADF images of VN films. **F.** HAADF image of the VN film illustrating the two areas where EELS analysis is performed (blue square within the VN column, and pink square between two columns)**. G.** Corresponding EELS spectra including both V-$L_{3,2}$ edge and O-K edge.

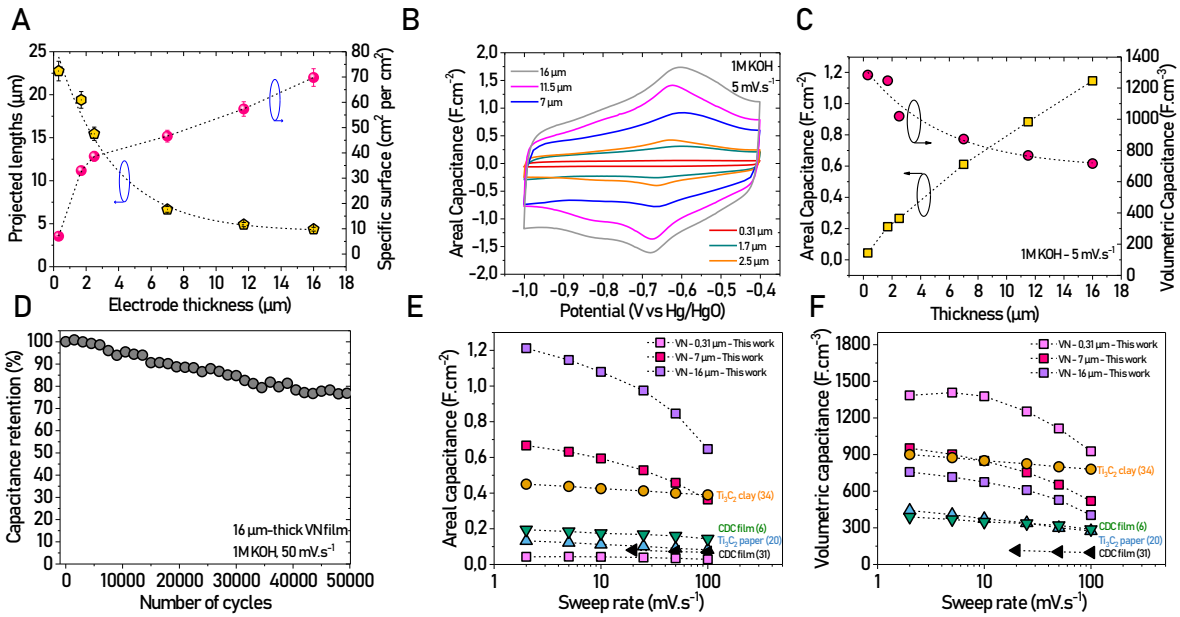

Figure 4 – Performance of the sputtered VN films. **A.** Evolution of the L_p and S_e vs the film thickness. **B.** CV plot of the VN electrode vs the thickness. **C.** Evolution of the areal and volumetric capacitances vs the thickness. **D.** Capacitance retention vs the number of cycles (16 µm-thick film) at 50 mV s^{-1}. **E/F**. Benchmarking the VN performance (square plots named "this work") as compared to state-of-the-art capacitive electrodes (**Fig. E:** areal capacitance, **Fig. F**: volumetric capacitance).

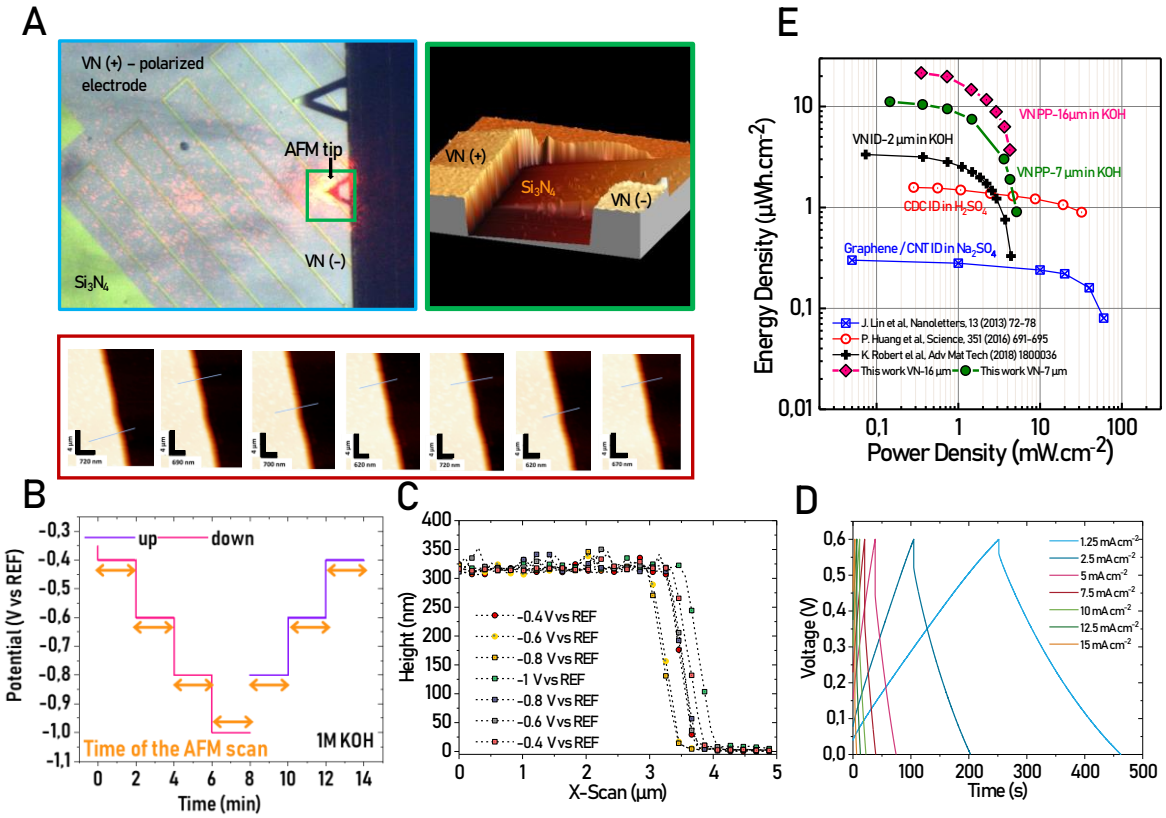

Figure 5 – A. *In situ* AFM analysis of a MSC in 1M KOH electrolyte. **B.** Plots of the potential vs time between -0.4 and -1 V vs Hg/HgO. **C.** Evolution of the VN height at different potentials. **D.** Charge / discharge profiles of a 16 µm-thick VN MSC at various current densities. **E.** Ragone plot of the MSCs in comparison to cutting-edge micro-devices operating in aqueous electrolyte.

References and notes

1 J.-M. Tarascon and M. Armand, *Nature*, 2001, **414**, 359–367.

2 A. Raj and D. Steingart, *J. Electrochem. Soc.*, 2018, **165**, B3130–B3136.

3 C. Lethien, J. Le Bideau and T. Brousse, *Energy Environ. Sci.*, 2019, **12**, 96–115.

4 C. Lethien, D. Troadec, P. Roussel, A. Demortière, E. Eustache, V. De Andrade, F. Vaurette, J. Freixas, T. Brousse, P. Tilmant, L. Morgenroth and M. Létiche, *Adv. Energy Mater.*, 2016, **7**, 1601402.

5 J. I. Hur, L. C. Smith and B. Dunn, *Joule*, 2018, **2**, 1187–1201.

6 P. Huang, P. L. Taberna, P. Simon, V. Turq, M. Respaud, C. Lethien, B. Chaudret, S. Pinaud, B. Daffos, R. Laloo, K. Brousse, A. Demortiere and Y. Gogotsi, *Science (80-.).*, 2016, **351**, 691–695.

7 M. F. El-Kady, V. Strong, S. Dubin and R. B. Kaner, *Science (80-.).*, 2012, **335**, 1326–1330.

8 D. Pech, M. Brunet, H. Durou, P. Huang, V. Mochalin, Y. Gogotsi, P.-L. Taberna and P. Simon, *Nat. Nanotechnol.*, 2010, **5**, 651–654.

9 J. Y. Hwang, M. F. El-Kady, Y. Wang, L. Wang, Y. Shao, K. Marsh, J. M. Ko and R. B. Kaner, *Nano Energy*, 2015, **18**, 57–70.

10 M. F. El-Kady, M. Ihns, M. Li, J. Y. Hwang, M. F. Mousavi, L. Chaney, A. T. Lech and R. B. Kaner, *Proc. Natl. Acad. Sci.*, 2015, **112**, 4233–4238.

11 E. Eustache, C. Douard, A. Demortière, V. De Andrade, M. Brachet, J. Le Bideau, T. Brousse and C. Lethien, *Adv. Mater. Technol.*, 2017, **2**, 1700126.

12 K. Robert, C. Douard, A. Demortière, F. Blanchard, P. Roussel, T. Brousse and C. Lethien, *Adv. Mater. Technol.*, 2018, **3**, 1800036.

13 B. E. Conway, in *Electrochemical Supercapacitors*, 1999, pp. 259–297.

14 M. Toupin, T. Brousse and D. Bélanger, *Chem. Mater.*, 2002, **14**, 3946–3952.

15 M. Toupin, T. Brousse and D. Bélanger, *Chem. Mater.*, 2004, **16**, 3184–3190.

16 H. D. Abruña, M. A. Lowe, P.-L. Taberna, B. Dunn, V. Augustyn, S. H. Tolbert, J. W. Kim, J. Come and P. Simon, *Nat. Mater.*, 2013, **12**, 518–522.

17 H. S. Kim, J. B. Cook, H. Lin, J. S. Ko, S. H. Tolbert, V. Ozolins and B. Dunn, *Nat. Mater.*, 2017, **16**, 454–462.

18 C.-H. Lai, D. Ashby, M. Moz, Y. Gogotsi, L. Pilon and B. Dunn, *Langmuir*, 2017, **33**, 9407–9415.

19 H. Sun, L. Mei, J. Liang, Z. Zhao, C. Lee, H. Fei, M. Ding, J. Lau, M. Li, C. Wang, X. Xu, G. Hao, B. Papandrea, I. Shakir, B. Dunn, Y. Huang and X. Duan, *Science (80-.).*, 2017, **356**, 599–604.

20 M. R. Lukatskaya, O. Mashtalir, C. E. Ren, Y. Dall'Agnese, P. Rozier, P. L. Taberna, M. Naguib, P. Simon, M. W. Barsoum and Y. Gogotsi, *Science (80-.).*, 2013, **341**, 1502–1505.

21 M. R. Lukatskaya, S. Kota, Z. Lin, M. Q. Zhao, N. Shpigel, M. D. Levi, J. Halim, P. L. Taberna, M. W. Barsoum, P. Simon and Y. Gogotsi, *Nat. Energy*, 2017, **6**, 1–6.

22 B. Anasori, M. R. Lukatskaya and Y. Gogotsi, *Nat. Rev. Mater.*, 2017, **2**, 16098.

23 T.-C. Liu, W. G. Pell, S. L. Roberson and B. E. Conway, *J. Electrochem. Soc.*, 1998, **145**, 1882.

24 D. Choi, G. E. Blomgren and P. N. Kumta, *Adv. Mater.*, 2006, **18**, 1178–1182.

25 O. Bondarchuk, A. Morel, D. Bélanger, E. Goikolea, T. Brousse and R. Mysyk, *J. Power Sources*, 2016, **324**, 439–446.

26 P. Huang, M. Létiche, M. Respaud, B. Chaudret, A. Demortière, K. Brousse, S. Pinaud, L. Buchaillot, P. Simon, P. L. Taberna, B. Daffos, P. Roussel and C. Lethien, *Adv. Funct. Mater.*, 2017, **27**, 1606813.

27 S. Ouendi, K. Robert, D. Stievenard, T. Brousse, P. Roussel and C. Lethien, *Energy Storage Mater.*, , DOI:10.1016/j.ensm.2019.04.006.

28 L. W. M. Lau, A. R. Gerson, B. P. Payne, R. S. C. Smart, M. C. Biesinger and A. P. Grosvenor, *Appl. Surf. Sci.*, 2010, **257**, 2717–2730.

29 T. Brousse, D. Bélanger and J. W. Long, *J. Electrochem. Soc.*, 2015, **162**, A5185–A5189.

30 P. Simon, Y. Gogotsi and B. Dunn, *Science (80-.).*, 2014, **343**, 1210–1211.

31 J. Chmiola, G. Yushin, Y. Gogotsi, C. Portet, P. Simon and P. L. Taberna, *Science (80-.).*, 2006, **313**, 1760–1763.

32 J. Chmiola, C. Largeot, P. L. Taberna, P. Simon and Y. Gogotsi, *Science (80-.).*, 2010, **328**, 480–483.

33 P. Simon, B. Daffos, C. Lethien, K. Brousse, S. Pinaud, P. Huang, M. Respaud, B. Chaudret and P. L. Taberna, *J. Power Sources*, 2016, **328**, 520–526.

34 M. Ghidiu, M. R. Lukatskaya, M.-Q. Zhao, Y. Gogotsi and M. W. Barsoum, *Nature*, 2014, **516**, 78–81.

35 T. M. Arruda, M. Heon, V. Presser, P. C. Hillesheim, S. Dai, Y. Gogotsi, S. V. Kalinin and N. Balke, *Energy Environ. Sci.*, 2013, **6**, 225–231.

Acknowledgments: This research benefitted from the financial support of the ANR within the DENSSCAPIO project (ANR-17-CE05-0015-02). The authors would also like to thank the ANR STORE-EX and the RS2E for their financial support. The RENATECH network receives our

utmost gratitude. XAS experiment was performed on the ROCK beamline at SOLEIL synchrotron, which is benefiting from a public grant overseen by the French National Research Agency as part of the “Investissements d’Avenir” program (Reference: ANR-10-EQPX-45). The authors declare no conflict of interest. All the authors wish to thank Anne Duchene for the sketch-up. KR achieved the deposition of VN films and the fabrication of on-chip MSCs. DS, DD and CL were involved in the *in situ* AFM analysis. KR, CD, AI, TB and CL were involved in the *operando* XAS. DT, MM, MH, PR and CL were involved in the TEM / EELS analysis of the VN films. KR, PS, NN and CL carried out the ToF SIMS / XPS analyses.